Ceramics International 45 (2019) 18871–18875

Contents lists available at ScienceDirect

Ceramics International

journal homepage: www.elsevier.com/locate/ceramint

Non-destructive optical second harmonic generation imaging of 3D printed aluminum nitride ceramics

Angela C. Aguilar[a], Carlos A. Diaz-Moreno[b], Alex D. Price[a], Rajen K. Goutam[a], Cristian E. Botez[c], Yirong Lin[b,d], Ryan B. Wicker[b,d], Chunqiang Li[a,*]

[a] Department of Physics, The University of Texas at El Paso, El Paso, TX, 79968, USA
[b] W. M. Keck Center for 3D Innovation, The University of Texas at El Paso, El Paso, TX, 79968, USA
[c] College of Science and Mathematics, School of Health Professions, Rowan University, Glassboro, NJ, 08028, USA
[d] Department of Mechanical Engineering, The University of Texas at El Paso, El Paso, TX, 79968, USA

ARTICLE INFO

Keywords:
Aluminum nitride
Second harmonic generation

ABSTRACT

Aluminum nitride (AlN) ceramics have attracted broad interest due to their potential applications in electronics. Additive manufacturing of ceramic components are rapidly advancing, could provide a new way of manufacturing over conventional methods. Non-destructive testing of 3D printed ceramic samples is an important step for quality control in manufacturing. Here we show that AlN ceramics show strong optical second harmonic generation (SHG) signals due to its wurtzite crystal structure. Microscopic SHG imaging can also examine the microscopy domains in AlN ceramics with submicron spatial resolution. This technique has the potential to be applied as a non-destructive testing method for examining 3D printed AlN ceramic components.

1. Introduction

Over the past decades aluminum nitride (AlN) has become a widely studied ceramic material due to its extremely interesting combination of high thermal conductivity, high temperature stability and low thermal expansion, excellent electrical insulation, and wide bandgap [1,2]. These properties made AlN a good candidate for a wide range of electronic applications, such as circuit substrate, heat dissipater, piezoelectric transducers, microwave devices, and deep ultraviolet light emitting diodes [3–6]. Sintering is the common approach to prepare high-quality polycrystalline ceramics. Low temperature sintering and hot isostatic pressing (HIP) of AlN are typically done with oxidized additives such as Y_2O_3 due to the high melting point of AlN (~2200 °C) [7]. During sintering, grain growth occurs most rapidly where additives are rich. Through the introduction of these additives, oxygen can exist in the ceramic in the lattice or in these grain boundaries that will slightly change the structure of AlN along with its optical properties [7,8]. With the recent rapid advance of additive manufacturing (AM) technology, ceramic component can now be processed by AM with debindering and sintering afterward [9,10].

Non-destructive testing (NDT) is an important step of quality control in manufacturing. NDT techniques such as ultrasonic testing, X-ray computed tomography, eddy currents, and electromagnetic testing can measure material properties and detect irregularities [11]. However, an NDT technology can examine solid with properties of high 3D spatial resolution and noncontact is still missing. Optical techniques have the advantage of high spatial resolution due to the short light wavelength in the submicrometer range. For instance, optical coherence tomography (OCT), which was developed for medical imaging purpose, has been applied as an NDT technique characterizing surfaces and interfaces in a variety of materials at the resolution of several microns [12]. To further improve the spatial resolution to submicron range, other optical microscopic imaging techniques need to be developed.

Optical second harmonic generation (SHG) is nonlinear optical process that can be used as a non-destructive probing technique to determine properties of surfaces, interfaces and structures where there is a lack of inversion symmetry [13–16]. Thus, SHG has been applied as an NDT technique that characterizes surfaces and interfaces in several ceramic materials with resolution of several microns [17,18]. Aluminum nitride has both second- ($\chi^{(2)}$) and third-order ($\chi^{(3)}$) nonlinear optical susceptibility due to its non-centrosymmetric crystal structure in its stable wurtzite phase [19]. In addition, AlN has an advantage of having one of the largest bandgaps (6.2 eV) among all known semiconductors. This wide bandgap not only provides suppression of two photon absorption, but also allows for wide band SHG from ultraviolet (UV) to infrared (IR) wavelengths [20]. Therefore, utilizing the

* Corresponding author.
E-mail address: cli@utep.edu (C. Li).

https://doi.org/10.1016/j.ceramint.2019.06.121
Received 8 April 2019; Accepted 12 June 2019
Available online 18 June 2019

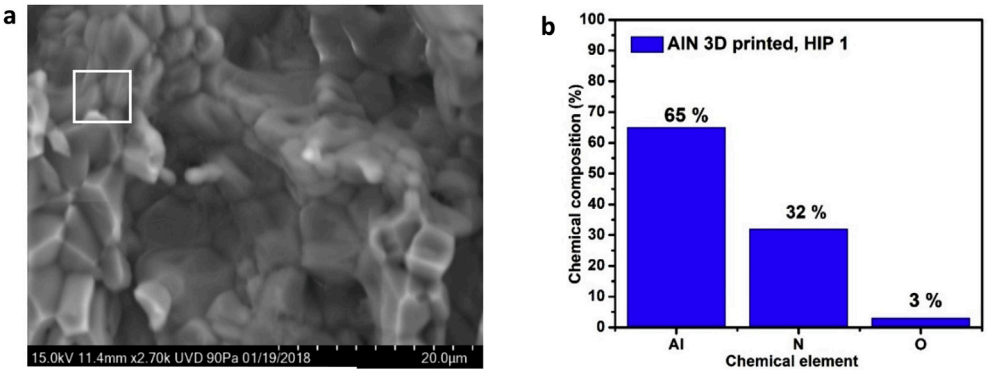

Fig. 1. a) SEM image of 3D printed AlN sample with HIP at 1900 °C. b) EDS results of this AlN sample.

nonlinear optical properties of AlN SHG imaging can determine orientations of grains, grain boundaries, and cavities inside [17,21]. Previous works on AlN optical properties have focused on thin films in both wurtzite and cubic phases, and there have been few experimental investigations on the nonlinear optical properties of AlN prepared by sintering, HIP, and AM [22–25]. Understanding the effects of these manufacturing processes and additives on the properties of AlN is important for tuning the ceramic for its applications such as 3D printed microchips or larger scaled structures. In this work we present SHG microscopic imaging of AlN ceramics prepared by binder jetting (BJ) subjected to HIP process. In the meantime, x-ray diffraction (XRD) and scanning electron microscopy (SEM) are used to characterize crystal structure and morphology.

2. Materials and methods

2.1. Materials processing

In this work, the AlN precursor powder was purchased from American Element®, with a measured purity of 99.9%. The powder had an average particle size of ~45 µm. AlN components were fabricated using binder jetting in an ExOne M-lab system followed by hot isostatic pressing. The HIP process used an AIP-30H furnace. The HIP consisted of a temperature ramp rate of 5 °C/min. The sample was holed at 1900 °C in a nitrogen pressurized atmosphere at 30,000 psi for 8 h. Details of AM and HIP processes were previously reported in Ref #8.

2.2. Optical second harmonic generation imaging

The SHG microscope was based on a two-photon microscope developed earlier [26]. In brief, the laser source is a mode-locked femtosecond Ti:Sapphire laser (Maitai HP, wavelength 690–1040 nm, 100 fs, 80 MHz, Spectra-Physics, Santa Clara, California). The wavelength was set at 940 nm to generate SHG signal at 470 nm. The blue detection channel has a bandpass filter (417–477 nm) to selectively detect this SHG signal. The laser power at the sample site was adjusted using a half waveplate and a polarizing beam splitter. The outputs of photo detectors were fed into a frame grabber (SolioseA/XA, Matrox, Quebec, Canada). Two-dimensional images in the x-y plane are acquired through a home-built software program. Each frame has 500 × 500 pixels. Each final static image is an average of 50 frames.

2.3. SEM-EDS

Morphology aspects and chemical analysis were performed by using a scanning electron microscopy SU3500 system (Hitachi, Japan) with an integrated energy-dispersive X-ray spectroscopy (EDS) Oxford Instrument X-Max^N (Oxford Instruments, UK).

2.4. X-ray diffraction

X-ray diffraction patterns of the powder samples were collected on a powder diffractometer (Empyrean 2, Malvern Panalytical, Netherlands) using a Cu K-α radiation source (λ = 1.54184 Å).

Debye ring patterns were collected on a Bruker D8 Quest SC XRD using a Mo K-α radiation source (λ = 0.71073 Å), all at room temperature. Debye ring patterns were integrated using Bruker's APEX 3 software. All powder diffraction patterns were refined and fitted with known patterns in the Inorganic Crystal Structure Database (ICSD) via Malvern's HighScore$^+$ software.

3. Results and discussion

3.1. SEM-EDS

SEM image was employed to characterize the morphological structure of AlN samples after HIP. During the HIP process trapped gases can evolve from the powder surface or the decomposition of binder can trap in closed pores. These processes make densification of materials difficult. It is well known that the post thermal processing for AlN is difficult to achieve due to its covalent nature. Fig. 1a shows a representative SEM image at the cross section of the AlN component that was subjected to the HIP process at 1900 °C. This image shows homogeneous sintered microparticles exhibiting coalescence with well-formed boundaries. The regions indicated with white rectangles were used for EDS chemical analysis. Fig. 1b demonstrates the EDS results, showing that the components subjected to the HIP cycle had a chemical trace corresponding to 65% Al, 32% N, and 3% O. This chemical composition obtained belongs to original atomic/mass of Al and N in AlN stoichiometric composition. The oxygen trace can be the result of trapped porous structures in the fabrication process.

3.2. XRD

To further study the phase of these AlN power samples, x-ray powder diffraction was performed with a Panalytical Empyrean 2 system using a Cu K-α source (λ = 1.54184 Å) in the 2θ range of 30°–90° (Fig. 2a). Though the patterns of both raw and 3D printed HIP AlN powder samples match that of wurtzite AlN as shown in ICSD (54697), it is possible that the pattern can be fit to sapphire (Al_2O_3) as shown in ICSD (173713). Since the common defects in AlN are oxides [7], these samples may contain some oxide impurities especially for heat treated sample as demonstrated in Fig. 1b. These samples were then run on a Bruker D8 Quest single crystal diffractometer. This system is equipped with a Mo K-α source (λ = 0.71073 Å), which could yield a different diffraction pattern between the nitride and oxide compounds. Debye ring patterns for each sample were acquired and then integrated to obtain peak patterns as shown in Fig. 2b and c respectively. In contrast to the Cu K-α patterns, the patterns obtained from the Mo K-α

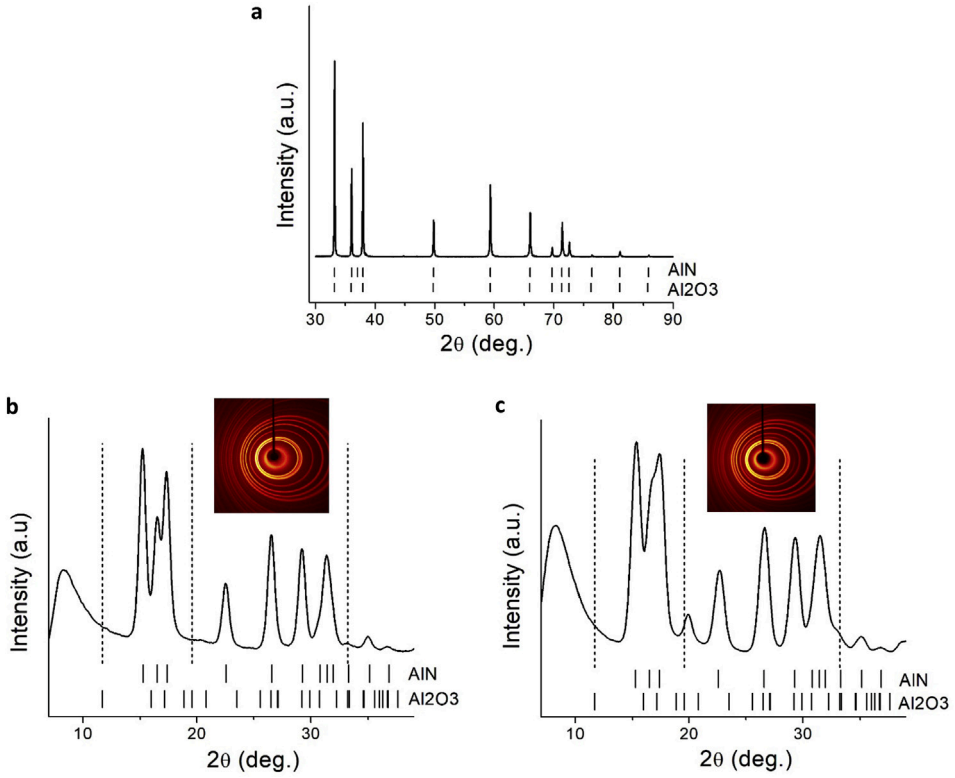

Fig. 2. a) Cu K-α XRD peaks of raw AlN sample. The solid line is the XRD scan, and vertical tick marks are reference peaks of AlN and Al_2O_3 respectively. b) Mo K-α XRD peaks of raw sample and Debye rings. c) Mo K- α XRD peaks of 3D printed HIP sample and Debye rings.

Table 1
Lattice parameters as found in the two AlN samples (raw and 3D printed HIP) through Rietveld refinement.

	a (Å)	b (Å)	c (Å)
raw	3.11175	3.11175	4.98090
3D HIP	3.11336	3.11336	4.98057

source shows slight deviations in pattern structure which are mapped to the presence of an oxide within the material. The 3D printed HIP sample (Fig. 2c) shows similar patterns to the raw sample (Fig. 2b) with several differences, such as the peak at about the 20° mark in 2θ. The broad peak below 10° is due to the x-ray beam scattering from the beam stop and is not related to the sample. Lattice parameters were obtained through Rietveld refinement. There are small differences in lattice parameters between the two samples as shown in Table 1.

3.3. Optical second harmonic generation imaging

Second harmonic generation is a second order nonlinear process, which indicates that the generated frequency-doubled signal intensity is proportional to the square of the intensity of the incident light. The samples were irradiated with varying laser powers ranging from 1 to 200 mW with increments of 5 mW. At each power level SHG images were taken. To quantify the dependence of SHG intensity on laser power, a region of interest (ROI) was chosen to cover the sample, and the average signal intensity in this ROI was measured. The SHG intensity vs. laser power curves are shown in Fig. 3a as log-log plots. The dash lines are the fitting curves for data points in the intermediate range without including the saturated signals in the high laser power region. The 3D printed HIP sample curve shows a slope of 2, which demonstrates the second order process nature of these SHG signals. The raw sample curve has a slope of 1.7, which may be due to defects in these raw materials, such as different crystal orientations arrangement in the powder form or possible agglomerations.

The SHG signal vector generated from a single phase crystal is determined by the product between the $\chi^{(2)}$ nonlinear susceptibility tensor of the material and the incident electric field vector. Therefore, when the polarization of the incident electric field is rotated, the SHG signal amplitude will change accordingly. In this experiment the incident laser beam polarization was rotated by a half wave plate before the beam enters the microscope. The wave plate was rotated from 0° to 180°, and the corresponding electric field was rotated from 0° to 360°, with a step size of 10°. At each angle an image was recorded. For each image the average SHG intensity of ROI was measured, and this SHG signal intensity vs. incident beam polarization is shown in Fig. 3b. Both raw and 3D printed HIP samples show a clear dependence SHG signal amplitude on the polarization of the electric field direction with dipole shapes, which indicates the wurtzite phase (space group $P6_3mc$) of both samples. The $\chi^{(2)}$ tensor for wurtzite phase structure has a general form [16]:

$$\chi^{(2)} = \begin{pmatrix} 0 & 0 & 0 & 0 & \chi_{15} & 0 \\ 0 & 0 & 0 & \chi_{24} & 0 & 0 \\ \chi_{31} & \chi_{32} & \chi_{33} & 0 & 0 & 0 \end{pmatrix}$$

Further quantifying the SHG signal intensity variation with respect to the incident beam polarization and crystal orientation can measure the matrix components [16]. Fig. 3c illustrates the SHG intensity as a function of the incident laser polarization from a raw AlN sample. At 0° and 180° of laser polarization the top right and bottom left domains show strong SHG signal, while the top left and bottom right domains show minimum SHG signal. At 90° and 270° such SHG intensity pattern is reversed. This result clearly shows the orientation of AlN domain pattern at high contrast, which can be utilized as a non-destructive characterization technique. Fig. 3d is a composite image of all images from Fig. 3c with green color representing 0° and 180° images, and red color representing 90° and 360°.

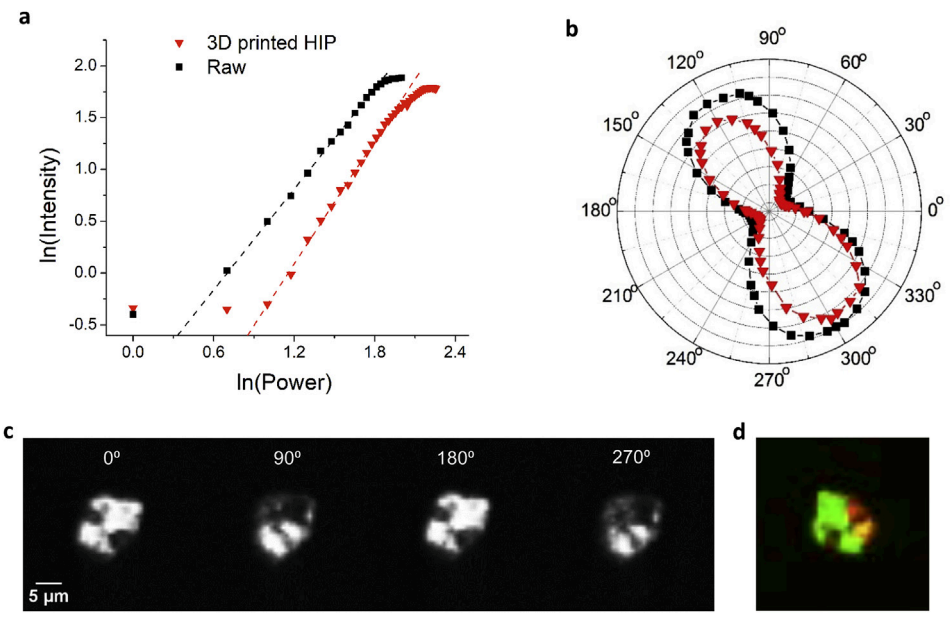

Fig. 3. a) Log-log plot of SHG signal intensity vs. laser power. b) Polar plots for SHG signals from AlN samples vs. incident laser beam polarization. c) Polarization-dependent SHG images of raw AlN samples d) Composite image, green color corresponds to 0° rotation, red color corresponds to approximately 90° rotation, the yellow color indicated overlap of phases. (For interpretation of the references to color in this figure legend, the reader is referred to the Web version of this article.)

4. Conclusion

We have examined the SHG response from AlN ceramics in both raw form and 3D printed form fabricated by binder jetting under different laser excitation power and laser polarizations. Energy-dispersive x-ray spectroscopy confirms the chemical composition of these samples, and x-ray diffraction confirms the wurtzite phase of both samples. Slight deviations in the lattice parameters in 3D printed HIP sample from raw sample can be attributed to oxidation during processing as shown in EDS and XRD results. Polar plots of SHG signals clearly show the dipolar behavior, which is typical for a wurtzite structure. Domain structures are clearly revealed in these microscopic SHG images by varying laser polarization. Therefore, this technique can be potentially used a non-destructive testing method to examine submicron details for 3D printed AlN ceramic components.

Acknowledgements

This work is supported by the US National Science Foundation (1429708, and 1827745). Carlos A. Diaz-Moreno thanks Mexico's Consejo Nacional de Ciencia y Tecnología (CONACYT) for support through Postdoctoral Abroad Program, Solicitation No. 250381 at The University of Texas at El Paso.

References

[1] H.-K. Lee, D.K. Kim, Investigation on thermal conductivity of aluminum nitride ceramics by FT-Raman spectroscopy, J. Am. Ceram. Soc. 93 (2010) 2167–2170 https://doi.org/10.1111/j.1551-2916.2010.03704.x.
[2] G.A. Slack, Nonmetallic crystals with high thermal conductivity, J. Phys. Chem. Solids 34 (1973) 321–335 https://doi.org/10.1016/0022-3697(73)90092-9.
[3] Y. Taniyasu, M. Kasu, T. Makimoto, An aluminium nitride light-emitting diode with a wavelength of 210 nanometres, Nature 441 (2006) 325 https://doi.org/10.1038/nature04760.
[4] Z.R. Song, Y.H. Yu, S.C. Zou, Z.H. Zheng, D.S. Shen, E.Z. Luo, Z. Xie, B. Sundaravel, S.B. Wong, I.H. Wilson, Simulation and characterization on properties of AlN films for SOI application, Thin Solid Films 459 (2004) 41–47 https://doi.org/10.1016/j.tsf.2003.12.091.
[5] C. Xiong, W.H.P. Pernice, X. Sun, C. Schuck, K.Y. Fong, H.X. Tang, Aluminum nitride as a new material for chip-scale optomechanics and nonlinear optics, New J. Phys. 14 (2012) 1–29 https://doi.org/10.1088/1367-2630/14/9/095014.
[6] H. Jung, H.X. Tang, Aluminum nitride as nonlinear optical material for on-chip frequency comb generation and frequency conversion, Nanophotonics 5 (2016) 263–271 https://doi.org/10.1515/nanoph-2016-0020.
[7] M. Vlasova, N. Kakazey, I. Rosales, L. Krushinskaya, A. Bykov, T. Tomila, E. Voitsehovskaya, V. Vinokurov, Synthesis of composite AlN-AlON-Al_2O_3 powders and ceramics prepared by high-pressure sintering, Sci. Sinter. 42 (2010) 283–295 https://doi.org/10.2298/SOS1003283V.
[8] J. Zhan, Y. Cao, H. Zhang, J. Guo, J. Zhang, C. Geng, X. Shi, S. Cui, W. Tang, Low-temperature sintering of AlN ceramics by Sm_2O_3-Y_2O_3-CaO sintering additives formed via decomposition of nitrate solutions, J. Mater. Eng. Perform. 26 (2017) 453–459 https://doi.org/10.1007/s11665-016-2453-1.
[9] C.A. Diaz-Moreno, C. Rodarte, S. Ambriz, D. Bermudez, D. Roberson, C. Terrazas, D. Espalin, R. Ferguson, E. Shafirovich, Y. Lin, R.B. Wicker, Binder jetting of high temperature and thermally conductive (aluminum nitride) ceramic, Proceedings of the 29th Annual International Solid Freeform Fabrication Symposium, 2018, pp. 143–159.
[10] W. Du, C. Ma, X. Ren, Z. Pei, Binder jetting additive manufacturing of ceramics: a literature review, Proceedings of the ASME 2017 International Mechanical Engineering Congress and Exposition, (2017), p. 70344 https://doi.org/10.1115/IMECE2017-70344.
[11] M. Fiebig, V.V. Palov, R.V. Pissarev, Second-harmonic generation as a tool for studying electronic and magnetic structures of crystals: review, J. Opt. Soc. Am. B 22 (2005) 96–118 https://doi.org/10.1364/JOSAB.22.000096.
[12] R. Su, M. Kirillin, E.W. Chang, E. Sergeeva, S.H. Yun, L. Mattsson, Perspectives of mid-infrared optical coherence tomography for inspection and micrometrology of industrial ceramics, Optic Express 22 (2014) 15804–15819 https://doi.org/10.1364/OE.22.015804.
[13] G. Lüpke, Characterization of semiconductor interfaces by second-harmonic generation, Surf. Sci. Rep. 35 (1999) 75–161 https://doi.org/10.1016/S0167-5729(99)00007-2.
[14] N. Watanabe, T. Kimoto, J. Suda, The temperature dependence of the refractive indices of GaN and AlN from room temperature up to 515 °C, J. Appl. Phys. 104 (2008) 10610 https://doi.org/10.1063/1.3021148.
[15] Y.R. Shen, Surface properties probed by second-harmonic and sum-frequency generation, Nature 337 (1989) 519–525 https://doi.org/10.1038/337519a0.
[16] R.W. Boyd, Nonlinear Optics, third ed., Academic Press, 2008.
[17] C.A. Díaz-Moreno, Y. Ding, C. Li, J. Portelles, J. Heiras, A. Hurtado-Macias, J.R. Farias, J. González-Hernández, M.J. Yacamán, J. López, Relaxor ferroelectricity, ferromagnetic and optical second harmonic properties in lanthanum lithium niobate ($La_{0.05}Li_{0.85}NbO_3$) nanoparticles, J. Magn. Magn. Mater. 433 (2017) 262–270 https://doi.org/10.1016/j.jmmm.2017.03.022.
[18] K.A. Brekhov, K.A. Grishunin, D.V. Afanas'ev, S.V. Semin, N.E. Sherstyuk, E.D. Mishina, A.V. Kimel, Optical second harmonic generation and its photoinduced dynamics in ferroelectric semiconductor $Sn_2P_2S_6$, Phys. Solid State 60 (2018) 31–36 https://doi.org/10.1134/S1063783418010080.
[19] J.L.P. Hughes, Y. Wang, J.E. Sipe, Calculation of linear and second-order optical response in wurtzite GaN and AlN, Phys. Rev. B 55 (1997) 13630–13640 https://doi.org/10.1103/PhysRevB.55.13630.
[20] M. Stegmaier, J. Ebert, J.M. Meckbach, K. Ilin, M. Siegel, W.H.P. Pernice, Aluminum nitride nanophotonic circuits operating at ultraviolet wavelengths, Appl. Phys. Lett. 104 (2014) 091108https://doi.org/10.1063/1.4867529.
[21] M. Timofeeva, A. Bouravleuv, G. Cirlin, I. Shtrom, I. Soshnikov, M. Reig Escalé, A. Sergeyev, R. Grange, Polar second-harmonic imaging to resolve pure and mixed crystal phases along GaAs nanowires, Nano Lett. 16 (2016) 6290–6297 https://doi.org/10.1021/acs.nanolett.6b02592.
[22] M. Alevli, C. Ozgit, I. Donmez, N. Biyikli, Optical properties of AlN thin films grown by plasma enhanced atomic layer deposition, J. Vac. Sci. Technol. A 30 (2012) 021506https://doi.org/10.1116/1.3687937.
[23] R.K. Choudhary, P. Mishra, R.C. Hubli, Optical properties of cubic AlN films grown by sputtering, Surf. Eng. 32 (2016) 304–306 https://doi.org/10.1179/1743294414Y.0000000399.

[24] F. Hajakbari, M.M. Larijani, M. Ghoranneviss, M. Aslaninejad, A. Hojabri, Optical properties of amorphous AlN thin films on glass and silicon substrates grown by single ion beam sputtering, Jpn. J. Appl. Phys. 49 (2010) 095802https://doi.org/10.1143/JJAP.49.095802.

[25] M.C. Larciprete, A. Bosco, A. Belardi, R. Li Voti, G. Leahu, C. Sibilia, E. Fazio, R. Ostuni, M. Bertolotti, Blue second harmonic generation from aluminum nitride films deposited onto silicon by sputtering technique, J. Appl. Phys. 100 (2006) 023507https://doi.org/10.1063/1.2219151.

[26] Y. Acosta, Q. Zhang, A. Rahaman, H. Ouellet, C. Xiao, J. Sun, C. Li, Imaging cytosolic translocation of Mycobacteria with two-photon fluorescence resonance energy transfer microscopy, Biomed. Opt. Express 5 (2014) 3990–4001 https://doi.org/10.1364/BOE.5.003990.